A generalized interpolation material point method for shallow ice shelves. Part II: anisotropic nonlocal damage mechanics and rift propagation

Alex Huth[1,†] , Ravindra Duddu[2,3] and Ben Smith[4]

[1]Department of Earth and Space Sciences, University of Washington, Seattle, WA, USA
[2]Department of Civil and Environmental Engineering, Vanderbilt University, Nashville, TN, USA
[3]Department of Earth and Environmental Sciences, Vanderbilt University, Nashville, TN, USA
[4]University of Washington, Applied Physics Laboratory, Polar Science Center, Seattle, WA, USA

Corresponding author: Alex Huth (ahuth@princeton.edu)

Key Points

- Our shallow-shelf creep damage model can represent the full evolution of ice shelf fracture from crevasse initiation to tabular calving
- Strongly anisotropic damage produces sharp rift patterns more consistent with observations than isotropic damage
- Conversely, zero-stress damage poorly captures rifting, but is easily modified to represent mass balance/necking effects. Necking mostly acts to heal damage.

[†] Current affiliation: Atmospheric and Oceanic Sciences, Princeton University, Princeton, NJ, USA

Abstract

Ice shelf fracture is responsible for roughly half of Antarctic ice mass loss in the form of calving and can weaken buttressing of upstream ice flow. Large uncertainties associated with the ice sheet response to climate variations are due to a poor understanding of these fracture processes and how to model them. Here, we address these problems by developing an anisotropic, nonlocal, creep damage model for large-scale shallow-shelf ice flow. This model can be used to study the full evolution of fracture from initiation of crevassing to rifting that eventually causes tabular calving. While previous ice shelf fracture models have largely relied on simple expressions to estimate crevasse depths, our model parameterizes fracture directly in 3-D. We also develop an efficient supporting numerical framework based on the material point method, which avoids advection errors. Using an idealized marine ice sheet, we test our methods in comparison to a damage model that parameterizes crevasse depths, as well as a modified version of the latter model that accounts for how necking and mass balance affect damage. We demonstrate that the creep damage model is best suited for capturing weakening and rifting, and that anisotropic damage reproduces typically observed fracture patterns better than isotropic damage. However, we also show how necking and mass balance can significantly influence damage on decadal timescales. Because these processes are currently absent from the creep damage parameterization, we discuss the possibility for a combined approach between models to best represent mechanical weakening and tabular calving within long-term simulations.

Plain Language Summary

Fracture of ice shelves decreases buttressing of grounded ice and accounts for approximately half of ice mass loss in Antarctica in the form of calving. Here, we introduce a damage modeling framework for large-scale shallow ice shelf fracture that is based on a creep damage approach used previously to model individual crevasses, where the accumulation and weakening effects of microcracks is calibrated to laboratory tests. Our damage model parameterizes fracture directly in 3-D, and in tensorial form to account for crevasse orientation. Using the material point methods from Part I, we maintain computational efficiency and avoid diffusion errors during damage advection. We demonstrate on an idealized ice configuration that our methods can represent fracture evolution ranging from crevasse initiation to rifting, and that anisotropic damage produces rift patterns that better match observations than isotropic damage. Furthermore, we show how a previously-proposed damage model that parameterizes crevasse depths is relatively ill-suited for capturing rifting; however, it can easily be modified to account for the effects of mass balance and necking on damage evolution, and we demonstrate that these processes have a significant impact on decadal timescales. We then discuss potential approaches for implementing these additional processes into the creep damage model.

1. Introduction

Fracture of ice shelves strongly impacts the evolution of the Antarctic Ice Sheet and its interaction with climate. Approximately half of ice mass loss is attributed to fracture-induced calving, while the other half is attributed to ocean-driven basal melting (Depoorter et al., 2013; Rignot et al., 2013; Paolo et al., 2015). Furthermore, mechanical weakening associated with fracture processes can decrease ice shelf buttressing of upstream grounded ice flow into the ocean, leading to sea level rise (e.g. Borstad et al., 2013; MacGregor et al., 2012). For example, the Antarctic glaciers that will likely contribute the most to sea level rise in the next centuries, Pine Island and Thwaites, are buttressed by ice shelves that contain only a limited region of ice that can be lost or weakened without dynamic consequences that would lead to increased mass loss from the grounded ice sheet (Fürst et al., 2016). In extreme cases, fracture can eliminate buttressing entirely if full ice shelf collapse occurs, as it did when the Larsen B Ice Shelf collapsed over a period of just 6 weeks in 2002, likely due to hydrofracture (Scambos et al., 2004) related to surface meltwater ponding enabled by rising surface air temperatures. Fracture is also interconnected with climate through ocean processes. Ocean driven basal-melting of ice shelves can cause thinning that makes ice shelves more vulnerable to fracture (Shepherd et al., 2003; Liu et al., 2015). In turn, calved tabular icebergs can alter ocean circulation (e.g. Robinson et al., 2020; Stern et al., 2015, 2016; Cougnon et al., 2017).

The importance of ice shelf fracture processes to ice sheet and climate dynamics motivates their incorporation into prognostic flow models of ice sheet-ice shelf systems to better assess ice shelf stability and project ice sheet response to climate change. An efficient, accurate, and commonly-used ice flow model for these systems is the Shallow Shelf Approximation (SSA), a 2-D vertically-integrated form of the incompressible Stokes equations. Prognostic representation of fracture in SSA models has ranged from simple calving parameterizations to explicitly modeling fracture evolution and its feedback on flow using damage variables. For calving alone, reasonable ice front positions have been obtained by parameterizing smooth calving rates (e.g. Alley et al., 2008; Levermann et al., 2012) or attempting to track crevasse depths over time, where crevasses are assumed to propagate to the depth where the horizontal Cauchy stress equals zero (e.g. Nye, 1957; Nick et al., 2010; Nick et al. 2013; Pollard et al., 2015). This “zero-stress” approach assumes crevasse depths are in equilibrium with the stress field, and has been further developed into damage models that may be used with the SSA (Sun et al., 2017; Bassis & Ma, 2015). Other SSA damage models do not explicitly track crevasse depths. For example, an SSA damage model was formulated by fitting a relationship between stress and damage fields inferred from observations of Larsen B Ice Shelf, but was mostly successful near the ice margins only and did not capture rifting (Borstad et al., 2016). Another

SSA damage model tested a variety of *ad hoc* measures for initiating fracture, but the approach was only sufficient for broadly capturing the feedback between flow dynamics and fracture-induced weakening (Albrecht & Levermann, 2012; Albrecht et al., 2014).

An alternative approach to the above models for parameterizing ice shelf fracture is to implement traditional creep damage mechanics, where damage generalizes the nucleation and accumulation of microcracks and their influence on flow (Lemaitre, 1992). A creep damage model of this type (Murakami and Ohno, 1980; Murakami, 1983; Murakami et al., 1988) has already been calibrated for ice flow according to laboratory data (Pralong & Funk, 2005; Pralong et al., 2006; Duddu & Waisman, 2012). This damage model is time-dependent, which allows better calibration to observed, dynamic fracture. Furthermore, the model may be implemented in isotropic or anisotropic form, where anisotropic damage is likely more consistent with the heavily-patterned fractures observed on ice shelves. While it has only been tested at the scale of individual crevasses and in isotropic form, this creep damage model has proved to be accurate enough to reasonably simulate two calving events in the Swiss Alps within a 2-D full-Stokes study (Pralong & Funk, 2005). Further progress with the isotropic creep damage model at similar spatial scales has included additional calibration for temperature dependence (Duddu & Waisman, 2012), nonlocal formulations (Duddu & Waisman, 2013; Duddu et al., 2013; Londono et al., 2017; Jimenez et al., 2017), and a modification to incorporate the effects of water pressure (Mobasher et al., 2016; Duddu et al., 2020). To our knowledge, only one study has considered parameterizing this damage model for application into SSA simulations of large-scale ice flow (Keller & Hutter, 2014). This study proposed updating the isotropic creep damage field in 3-D using parameterized Cauchy stresses, and vertically-averaging a 3-D damage-modified viscosity parameter for implementation into the 2-D SSA solution. However, this parameterization remains untested, potentially due to the inhibiting computational expense and complexity of actually implementing such a parameterization within existing ice flow models.

The overarching goal of this paper is to develop an SSA creep damage parameterization and modeling framework that can be used to represent the entire progression of ice shelf fracture, from initiation and evolution of subcritical damage to propagation of sharp rifts and calving of tabular icebergs. Our approach builds on the SSA parameterization proposed by Keller and Hutter (2014). We modify the model for an anisotropic creep damage variable, and construct a supporting numerical framework that minimizes error and maximizes efficiency so that it may be applied effectively within large-scale ice flow simulations. We adapt several schemes for this framework that improve model performance and physical consistency, including extension of the damage variable to nonlocal form, adaptive time-stepping based on damage accumulation, brittle rupture criteria, and numerical treatment once maximum damage is reached. The damage model is implemented within our generalized interpolation material point method (GIMPM) code, a hybrid Lagrangian-Eulerian particle variation of the finite element method (Huth et al., 2020). Traditional Eulerian ice flow models are subject to artificial diffusion when advecting the damage field (e.g. Albrecht & Levermann, 2014; Borstad et al., 2016), whereas this error is avoided when using our GIMPM-SSA model, thereby allowing sharpness of cracks to be preserved regardless of flow. Additionally, the GIMPM-SSA model drastically increases the computational efficiency of advecting the 3-D damage field, or any other 3-D field such as temperature.

We test the SSA creep damage model on an idealized marine ice sheet system (Asay-Davis et al., 2016) to demonstrate that it can capture all damage growth from initial accumulation to sharp rifting and tabular calving, and to conduct parameter sensitivity tests. We show, for example, that high level of creep damage anisotropy results in rifting more consistent with the sharp, arcuate patterns observed on ice shelves. Furthermore, we compare the performance of our model with two previously-proposed crevasse-depth-based damage models (Sun et al., 2017; Bassis & Ma, 2015), which we also extend from isotropic to anisotropic form. These comparisons clarify the physical relationships between the damage models and the numerical advantages of our framework. We confirm that the creep damage model is better suited for capturing initiation of damage, rifting, and calving. However, only the Bassis and Ma (2015) damage model accounts for the impact of mass balance and necking processes, and we discuss how these processes may alter damage evolution significantly, especially regarding damage healing over decades. Thus, we conclude that a combined approach between the two models may be a viable approach for accurately simulating large-scale ice shelf fracture processes on decadal timescales, which will be the focus of a future paper. The outline of this paper is as follows: in Section 2 we summarize the governing equations, including the SSA and damage parameterization; in Section 3 we detail the implementation of the damage model; in Section 4 we present the idealized ice sheet experiments; in Section 5 we discuss the results and potential future developments and applications; and in Section 6 we offer concluding remarks.

2. Governing Equations

We begin this section by briefly reviewing the SSA equations. Then, we present the creep damage model and its parameterization for the SSA. We use a mix of tensorial and indicial notation as needed for conciseness or clarity. Vectors are donated as $a = a_i \hat{e}_i$, where the indicial notation of the right-hand side is framed within a Cartesian coordinate system ($x_1, x_2, x_3) = (x, y, z)$, where i are the spatial indices and $\hat{e}_i$ are the orthonormal basis vectors. Second-order tensors are similarly denoted as $A = A_{ij} \hat{e}_i \otimes \hat{e}_j$, where $\otimes$ is the dyadic product of two vectors. We assume Einstein's convention of summation that repeated indices imply summation. Principal values of A are written as $\langle A_i \rangle$, where in this case, index i indicates principal components rather than Cartesian directions. Variables at time step m are indicated using the superscript A^m.

2.1. Shallow Shelf Approximation

Ice streams and ice shelves have little or no basal friction, so vertical shear is negligible. Consequently, horizontal velocities and the corresponding strain-rates can be assumed constant with depth. Excluding vertical shear components from the incompressible Stokes equations and vertically integrating yields the 2-D shallow shelf approximation, or SSA (MacAyeal, 1989; Weis et al., 2001)

$$\frac{\partial T_{ij}}{\partial x_j} + (\tau ¿¿ b)_i = \rho g H \frac{\partial s}{\partial x_i}, ¿ \tag{1}$$

where i ranges over $\{1,2\}$ to indicate the horizontal $x_1 - x_2$ plane, ρ is ice density, g is acceleration due to gravity, H is ice thickness, s is surface height above sea level, $\tau_{b,i}$ are the components the shear stress vector tangential to the glacier base, and T_{ij} is the vertically-integrated stress tensor

$$T_{ij} = 2\bar{\eta} H \left(\dot{\varepsilon}_{ij} + \left(\dot{\varepsilon}_{11} + \dot{\varepsilon}_{22} \right) \delta_{ij} \right). \tag{2}$$

In (2), $\dot{\varepsilon}_{ij}$ is the strain rate tensor and $\bar{\eta}$ is the depth-averaged viscosity

$$\bar{\eta} = \frac{1}{2} \bar{B} \dot{\varepsilon}_e^{\frac{1-n}{n}}, \tag{3}$$

where, $\dot{\varepsilon}_e$ is the scalar effective strain rate, n is Glen's Law exponent set to $n = 3$, and $\overline{B}$ is the depth-averaged flow rate factor. At the ice-ocean boundary (or ice front), the sea water pressure is applied using a depth-integrated Neumann boundary condition as

$$\int_b^s \sigma_{ij} \hat{n}_j \, dz = ¿ - \frac{1}{2} \rho_w g b^2 \hat{n}_i , ¿ \tag{4}$$

where σ is the Cauchy stress, $\hat{n}$ is the unit (outward) normal to the ice front, ρ_w is sea water density, and b is the elevation of the ice shelf base below sea level (Morland & Zainuddin, 1987). The SSA is solved for the in-plane velocity components (v_1, v_2) of the ice shelf/stream by reformulating (1) and (2) in terms of the velocity gradients derived from the strain rate tensor

$$\dot{\varepsilon}_{ij} = \frac{1}{2}\left(\frac{\partial v_i}{\partial x_j} + \frac{\partial v_j}{\partial x_i}\right).$$

2.2. Physical notion of continuum damage

We implement the anisotropic creep damage model originally proposed by Murakami and Ohno, (1980) and Murakami (1983,1988) for polycrystalline metals. Pralong and Funk (2005) first calibrated this model for glacier ice and discussed the thermodynamic considerations in Pralong et al. (2006). Damage is represented as a real-valued, symmetric second-order 3-D tensor, **D**, so that anisotropy is restricted to an orthotropic description where damage is tracked on three mutually perpendicular planes. The damage tensor has three real principal values, $\langle D_i \rangle$, each representing the ratio of the area of cracks or voids to the originally undamaged area along the principal plane with a normal corresponding to principal direction i (Murakami, 1983; Duddu & Waisman, 2013). This physical or geometric interpretation is valid under isotropic

$(\langle D_1\rangle = \langle D_2\rangle = \langle D_3\rangle)$ and orthotropic damage (Qi & Bertram, 1999). Each principal damage component is bounded by $0 \leq \langle D_i \rangle \leq D_{max}$, where a material point is undamaged if all $\langle D_i \rangle = 0$ and fully damaged if any $\langle D_i \rangle = D_{max}$. Setting D_{max} to the maximum possible value of unity corresponds to complete loss of strength, though numerically, D_{max} must be set less than unity to prevent the SSA from becoming an ill-posed problem. Given the plug-flow regime of the SSA, we assume that the damage tensor is oriented so that one principal component, which we denote as $\langle D_3 \rangle$, always aligns with the vertical x_3 axis ($\langle D_3 \rangle = D_{33}$¿. The other two principal axis lie in the horizontal $x_1 - x_2$ plane, where we always ensure $\langle D_1 \rangle \geq \langle D_2 \rangle$. Because vertical shear stress components are zero in the SSA, the orthotropic damage tensor has only four non-zero components D_{11},D_{22}, D_{33}, and D_{12} that need to be determined.

The damage evolution function and incorporation of the damage tensor into the SSA rely on the principle of strain equivalence (Lemaitre, 1971; Lemaitre & Chaboche, 1978). This principle states that strain is identical for a damaged state under the applied stress, σ_{ij} (force per area of ice, including voids), as for its undamaged state under the effective stress, $\tilde{\sigma}_{ij}$ (force per ice area, ignoring any voids). A linear transformation between the two stress spaces that ensures the symmetry of the effective stress tensor can be written as

$$\tilde{\sigma} = \frac{1}{2}\left[(I - D)^{-1}\sigma + \sigma(I - D)^{-1}\right], \tag{5}$$

where I is the second-order identity tensor. The effective deviatoric stress may be defined as (Pralong and Funk, 2005; Pralong et al., 2006)

$$\tilde{\sigma}^{D} = \frac{1}{2}\left[(I - D)^{-1} \sigma^{D} + \sigma^{D} (I - D)^{-1} \right]^{D}. \tag{6}$$

An effective strain-rate is used to incorporate damage into the constitutive relation and calculate the applied stress, and takes the form

$$\tilde{\dot{\varepsilon}} = \frac{1}{2}\left[(I - D)\dot{\varepsilon} + \dot{\varepsilon}(I - D) \right]^{D}. \tag{7}$$

2.3. Damage evolution function

The creep damage evolution function is expressed in rate form. While some SSA damage models assume damage updates instantaneously with the stress field in a brittle manner (e.g. Sun et al., 2017), a rate form is consistent with laboratory experiments on ice (Duddu &Waisman, 2012). Moreover, the creep damage model can be tuned to capture the time-dependent propagation of rifts in ice shelves based on satellite observations, and has numerical advantages related to adaptive time-stepping and extending the damage model to nonlocal form (Section 3). In the Lagrangian framework, we express the material derivative of the second-order creep damage tensor as the Jaumann derivative (Pralong & Funk, 2005)

$$\dot{D} = \frac{\partial D}{\partial t} = f + WD - DW, \tag{8}$$

where t is time, **W** is the spin tensor $W_{ij} = \frac{1}{2}\left(\frac{\partial v_i}{\partial x_j} - \frac{\partial v_j}{\partial x_i} \right)$, and **f** is the dynamic damage evolution function as (Murakami, 1988)

$$f = B^{\text{¿}} \left\langle \left\langle \chi - \sigma_{th} \right\rangle \right\rangle^{r} \left\{ Tr\left[(I - D)^{-1} \cdot \left(v^{(1)} \otimes v^{(1)} \right) \right] \right\}^{k} \left[(1 - \gamma) I + \gamma v^{(1)} \otimes v^{(1)} \right], \tag{9}$$

$$\chi = \alpha \langle \tilde{\sigma}_1 \rangle + \beta \sqrt{3 II_{\tilde{\sigma}^D}} + (1 - \alpha - \beta) I_{\tilde{\sigma}}. \quad (10)$$

In (9), $B^{¿}$, r, k are creep damage parameters (listed in Table 1) and χ is the Hayhurst stress, which is an equivalent stress measure defined in (10) (Hayhurst, 1972). The Hayhurst stress is a weighted combination of the maximum effective principal stress (weighted byα), the effective von Mises stress (weighted by β), and the effective hydrostatic stress (weighted by $\lambda = 1 - \alpha - \beta$). The terms $I_{\tilde{\sigma}}$ and $II_{\tilde{\sigma}^D}$ denote the first invariant of the effective Cauchy stress and the second invariant of the effective deviatoric stress, respectively. The Hayhurst weights must fulfill

$$0 \leq \alpha, \beta, \lambda \leq 1, \quad (11)$$

which we take as $\alpha = 0.21$, $\beta = 0.63$, and $\lambda = 0.16$ as previously calibrated from laboratory data (Pralong and Funk, 2005). The first term in (9) determines the damage evolution rate based on the Hayhurst criterion and σ_{th}, an assumed stress threshold that restricts damage evolution to where$\chi > \sigma_{th}$. The Macaulay brackets $\langle\langle \cdot \rangle\rangle$ are defined as

$$\langle\langle x \rangle\rangle = \begin{cases} x, \wedge if\ x \geq 0 \\ 0, \wedge if\ x < 0 \end{cases}. \quad (12)$$

In the second and third terms of (9), $v^{(1)}$ is the eigenvector corresponding to the maximum effective principal stress, $\langle \tilde{\sigma}_1 \rangle$, which we always assume lies within the horizontal $x_1 - x_2$plane to be consistent with crevasse formation along vertical planes. Operator $Tr[\cdot]$ denotes the trace. Parameter k has been calibrated based on

Table 1.
Parameters used in the creep damage experiments

laboratory experimental data to be a function of the Duddu & Waisman, 2012), but we set it to a constant here for simplicity. The second term of (9) accounts for the increase in the damage rate at a spatial location based on any pre-existing damage on the principal plane normal to the $v^{(1)}$ direction. The third term sets the level of anisotropy in damage accumulation according to the anisotropy weighting parameter γ, which can be set between zero (purely isotropic with damage accumulating on all principal planes equally) and one (purely anisotropic with damage accumulating only on the principal plane normal to the $v^{(1)}$ direction). If D and $\tilde{\sigma}$ are always coaxial, the relationship between the principal components of the damage rate is controlled by the anisotropy parameter as

$$\langle \dot{D}_2 \rangle = \langle \dot{D}_3 \rangle = (1-\gamma) \langle \dot{D}_1 \rangle. \tag{13}$$

Any misalignment between D and $\tilde{\sigma}$ will cause damage accumulation to become more weighted towards $\langle D_2 \rangle$ at the expense of $\langle D_1 \rangle$. Misalignment can occur, for example, as a rift develops and causes the orientations of principal stresses to change downstream. Note that in the case of full anisotropy (γ=1), Equation (9) will never produce damage on $\langle D_3 \rangle$, because we always assume the maximum effective principal stress lies within the horizontal $x_1 - x_2$plane. We test sensitivity to γ in Section 4.2.

2.4. Parameterization of creep damage for the SSA

While the SSA is 2-D, creep damage evolution requires the evaluation of the full Cauchy stress tensor in 3-D. Damage can then be vertically averaged for incorporation into the next SSA solution step (Section 3.3). The 3-D deviatoric stress tensor from the 2-D velocity field defined by the SSA with damage can be obtained at vertical coordinate z using the nonlinearly viscous constitutive relation for ice flow (Glen, 1955)

$$\sigma^{D}(z) = 2\eta(\dot{\varepsilon}_e)\tilde{\dot{\varepsilon}}(z), \tag{14}$$

where $\tilde{\dot{\varepsilon}}$ is determined according to (7) using the 2-D strain-rates from the SSA solution and the local 3-D damage. Subtracting the pressure, p, from the deviatoric stresses yields the needed Cauchy stresses ($\sigma_{ij} = \sigma_{ij}^{D} - p_i \delta_{ij}$), but pressure is unknown in the SSA. Keller and Hutter (2014) therefore proposed parameterizing an effective pressure, given as

$$p_{eff} = p_i - p_w, \tag{15}$$

where p_i is the ice pressure according to the hydrostatic approximation

$$p_i(z) = \rho g(s - z) - \sigma_{11}^{D}(z) - \sigma_{22}^{D}(z), \tag{16}$$

and p_w is the basal water pressure

$$p_w(z) = \begin{cases} 0, \wedge if\ z \geq z_{sl} \\ \rho_w g(z_{sl} - z), \wedge if\ z < z_{sl} \end{cases}, \tag{17}$$

where z_{sl} is sea level elevation, which we set to zero. Furthermore, these authors proposed that pressure should be unaffected by damage, with the justification that volumetric effects oppose crack formation because they are largely dominated by the compressive ice overburden. Consequently, the effective stress is calculated as $\tilde{\sigma}_{ij} = \tilde{\sigma}_{ij}^{D} - p_{eff}\delta_{ij}$ rather than as given in Equation (5), and the Hayhurst criterion (10) is re-expressed as

$$\chi_{SSA}=\alpha\left(\left\langle\tilde{\sigma}_1^D\right\rangle-p_{eff}\right)+\beta\sqrt{3\,II_{\tilde{\sigma}^D}}+\lambda\left(-3\,p_{eff}\right). \tag{18}$$

We test this scheme as given, but acknowledge that improvements to this parameterization are possible, especially regarding the basal water pressure term in (17). This term is overly simplistic for grounded ice; for example, Equation (17) assumes basal water pressure is zero for ice grounded above sea level, which may not be true in all cases. However, our focus here is largely on shelf ice, so we implement the parameterization as given. We also note that within a full-Stokes setting, water pressure has been incorporated into damaged ice using a poromechanics approach (Mobasher, et al., 2016; Duddu et al., 2020). A similar approach could potentially be adapted for the SSA parameterization.

3. Implementation

We start this section by discussing the GIMPM-SSA framework, including how damage is implemented within it and its advantages concerning accuracy and efficiency of the ice flow and damage solutions. We then present the solution for the local 3-D damage increment, and explain how it can be used to set an adaptive time step and diffused over a characteristic length scale to calculate a nonlocal damage increment. Furthermore, we describe a brittle rupture criterion, the depth-averaging of the 3-D damage field, and our current treatment of fully-damaged material points (rifts). Lastly, we detail incorporation of the depth-averaged damage variable into the SSA solution.

3.1. Generalized interpolation material point method (GIMPM)

If using mesh-based numerical methods, then artificial diffusion errors may arise during advection of the damage variable, which smear sharp edges and makes critical features such as rifts difficult to capture. This diffusion is inherent to purely Eulerian advection schemes, where the mesh is not moved with the computed velocity field, and can also arise when working in a Lagrangian frame (moving-mesh) due to frequent remeshing that may be required when modeling large-deformation materials like large-scale ice flow. While our creep damage model may be adopted for any flow-modeling framework, we implement it here within our GIMPM-SSA code to avoid these diffusion errors (Huth et al., 2020). The GIMPM (Bardenhagen & Kober, 2004) is one of several material point methods, which all share the same basic procedure. In the GIMPM, a set of material points (or particles) provides a Lagrangian description of the material domain and holds all dynamic variables. The momentum equations are solved on a background grid in a similar manner to the finite element method, but with the material points serving as moving integration points. The grid solution is then used to update material point quantities such as position, velocity, and area, as well as material point history variables. Here, the history variables are ice thickness and damage. These updates are performed in a Lagrangian frame, which ensures that all fields advect without diffusion errors and enables tracking of the ice front and grounding line at sub-grid accuracy. The primary difference between the various material point methods concerns the shape functions used to map between material points and the grid. The most accurate variants use C^1 continuous shape functions to ensure smooth transfers of stiffness as material points move between grid cells, and in the GIMPM, such shape functions are assembled by convolving linear grid functions with characteristic functions associated with each material point.

Within the GIMPM-SSA framework, we track damage and any other 3-D fields, such as temperature, upon a series of vertical layers assigned to each material point. For mesh-based methods, the vertical layers could be assigned to nodes or quadrature points instead. For the simulations in this paper, we always maintain an even distribution of layers between the local ice base and surface elevations, which is possible because we do not incorporate mass balance processes such as surface and basal melt, or infill of crevasses with snow at the surface or marine ice at the base. Furthermore, we do not account for necking processes (Bassis & Ma, 2015), and do not implement healing because the simulations here are largely tensile, though healing models have been proposed (Pralong & Funk, 2005; Pralong et al., 2006). Modifying the creep damage model to account for the impacts of mass balance, necking, and healing is beyond the scope of this paper. However, in Section 4.4, we test a damage model for comparison that does account for some of these processes (Bassis & Ma, 2015), and we discuss the potential for a combined approach between the models in Section 5.

3.2. Local 3-D damage increment

The 3-D damage updates take the form

$$D^{m+1} = D^m + \Delta D^m, \tag{19}$$

where ΔD^m is the damage increment over a time step and may be expressed in local or nonlocal form. For each material point layer, the local damage increment, ${}^{loc}\Delta D^m$, is found by integrating the damage evolution rate, $\dot{D}^m$, over the length of the time step Δt using the Runge-Kutta-Merson (RKM) method as detailed in Zolochevsky et al., 2009 and Ling et al., 2000. The RKM update allows higher accuracy and larger time steps than a forward Euler update. During the RKM scheme, an internal damage variable is continuously updated over a series of sub-steps, whose sizes are optimized for speed and accuracy. The strain-rate determined from the preceding SSA solution is unchanged during the RKM update. The damage rate is calculated by solving

Equations (7),(14),(6),(16),(17),(15),(9),(10), and (8). At completion, the RKM routine returns the local damage, ${}^{loc}D^{m+1}$, from which ${}^{loc}\Delta D^{m}$ can be calculated as ${}^{loc}\Delta D^{m} = {}^{loc}D^{m+1} - D^{m}$.

We stop damage accumulation on a layer once the maximum principal damage component reaches D_{max}, though further evolution via the spin terms in (8) is allowed. A damage component that reaches D_{max} is considered ruptured, and can roughly be associated with the formation of macrocracks or crevasses, though we currently make no explicit assumptions concerning their width, spatial distribution, or potential influence on driving stress. However, our parameterization is probably most consistent with widely-spaced crevassing, given that we do not modify stresses at depth to account for stress shielding from damaged layers of neighboring material points. Stopping damage accumulation once $\langle D_1 \rangle = D_{max}$ is a requirement of the current formulation of the damage model, which does not currently account for multi-axial damage accumulation after rupture. Therefore, our model does not currently allow development of cross-cutting crevasses, though we estimate their occurrence and influence on flow is typically minimal for ice shelves. However, multi-axial damage accumulation before rupture, which may occur under biaxial tension, could possibly be accounted for by modifying the anisotropy parameter according to the relative magnitude of the two tensile principal effective stresses (Ganczarski & Skryzypek, 2001). This multi-axial modification has yet to be verified for ice, and has minimal impact on the experiments presented here. Therefore, we present the results that did not use this modification.

We split the above solution for the 3-D damage increments into 2 loops over the layers of a material point. The first loop is run from the bottom layer towards the top layer, and is exited if a layer is encountered with ${}^{loc}\Delta D^{m} = 0$ and $D^{m} = 0$ for all components. If the first loop does not process all layers, a second loop from the surface towards the base is initiated with the same exit criterion. During the second loop, we assume damage is associated with surface crevassing and ignore the sea water pressure term in the effective pressure. A surface meltwater pressure term could be added, instead. This two-loop scheme assumes cracks will not initiate in the middle of the shelf, and consequently, we achieve a faster solution by avoiding processing layers that will remain undamaged.

3.3. Adaptive time stepping

The maximum change in vertically-averaged local damage, $\overline{dD}_{max}$, of all material points is used to adjust the time step as needed for both the current and next computational cycle, with the goal of limiting the amount of damage allowed to accumulate each cycle to ensure accuracy, stability, and efficiency. Because the damage update can affect the current time step, it must begin each computational cycle. We define $\overline{dD}_{max}$ as

$$\overline{dD}_{max} = max\left(\left\langle {}^{loc}\overline{D}^{m+1}\right\rangle - \left\langle \overline{D}^{m}\right\rangle\right), \tag{20}$$

where '*max*' on the right hand side indicates the maximum value of all principal components, and vertical averaging of the damage variables takes the form

$$\overline{D} = \frac{\int_b^s D(z)\,B(z, T^{¿})\,dz}{\int_b^s B(z, T^{¿})\,dz}, \tag{21}$$

where $T^{¿}$ is temperature, on which the 3-D flow-rate factor, $B(z, T^{¿})$, is dependent. The integrals are evaluated using the trapezoid rule. Note that since $B(z, T^{¿})$ can vary with depth, it must be included in (21) alongside $D(z)$ to properly capture the combined effect of damage and thermal softening on the depth-averaged viscosity of ice (Keller & Hutter, 2014).

If $\overline{dD}_{max} \geq 0.075$, we decrease the current time step as $\Delta t^m = \Delta t^m / 1.5$ and recalculate the local damage increments. This situation rarely occurs, but serves as a safeguard against rapidly increasing damage. If $\overline{dD}_{max} < 0.075$, the time step for the next computational cycle is set as

$\Delta t^{m+1} = min\left(\delta_1 \Delta t^m, \dfrac{\delta_2 \Delta t^m}{\overline{dD}_{max}}, CFL\right)$, where we take $\delta_1 = 1.8$ and a δ_2 of 0.05 (Ling et al., 2000), and

$CFL = \delta_3 / max\left(\left|\dfrac{v_1}{\Delta x_1}\right| + \left|\dfrac{v_2}{\Delta x_2}\right|\right)$ indicates the maximum timestep that satisfies the Courant-Friedrichs-Lewy condition with constant $\delta_3 \leq 1$. Here, the time step is almost always restricted by damage rather than the CFL condition, and consequently, $\overline{dD}_{max} \approx \delta_2$ each computational cycle. The typical time increment varies based on the chosen damage parameters, but in all the simulations in this paper, it is on the order of days for sub-critical damage accumulation to hours during rapid rift propagation.

3.4. Nonlocal 3-D damage increment

Implementing nonlocal damage is motivated by both physical and numerical considerations. Physically, the progressive accumulation of microcracks that damage mechanics describes is distributed over a characteristic length scale in quasi-brittle materials like glacier ice (Bazant, 1986; Hall & Hayhurst, 1991). Numerically, local damage models suffer from directional mesh bias and mesh size sensitivity as damage localizes to single elements. We implement a nonlocal integral scheme (Duddu & Waisman, 2013), which diffuses the local damage increment between neighboring material points over the characteristic length scale. Note the difference between this intentional diffusion and the artificial diffusion that may arise using mesh-based advection schemes: the nonlocal damage diffusion is physically-based on observations of fracture in quasi-brittle materials, whereas artificial diffusion is a numerical error causes ice to lose damage unphysically over time.

Here, we apply the nonlocal scheme within each layer of neighboring material points. For example, local damage of the second layer of a material point is only reweighted according to the local damage of the second layer from surrounding material points, but not the layer above or below it. The nonlocal damage increment, $\Delta D^m\left(x^m\right)$, is calculated as

$$\Delta D^m\left(x^m\right)=\frac{\sum_{j=1}^{N}\phi\left(x^m-\hat{x}_j^{\,m}\right){}^{loc}\Delta D^m\left(\hat{x}_j^{\,m}\right)}{\sum_{j=1}^{N}\phi\left(x^m-\hat{x}_j^{\,m}\right)}, \tag{22}$$

where N is the number of material points, $\hat{x}_j^{\,m}$, positioned within a characteristic length, l_c, of x^m at timestep m. The weight function, ϕ is a Gaussian curve given as

$$\phi\left(x^m-\hat{x}_j^{\,m}\right)=\exp\left(-\left(\frac{\kappa\left\|x^m-\hat{x}_j^{\,m}\right\|}{l_c}\right)^2\right), \tag{23}$$

where constant κ controls the rate of decay of the weight function. We use $\kappa = 2$. The nonlocal length, l_c, should reflect the size of the fracture process zone and should be set so that the number of neighboring material points, j, is large enough to alleviate grid dependence (Duddu & Waisman, 2013). We note that as an alternative to the nonlocal integral scheme presented here, an implicit-gradient nonlocal scheme could be implemented, instead (Jimenez et al., 2017).

However, the gradient approach requires solving an equation on the mesh for each layer, and is therefore more computationally expensive.

3.5. 3-D damage update

On each material point layer, the 3-D damage tensor is updated from the damage increment according to (19). Afterwards, a brittle rupture or failure criterion is enforced, where if the principal value $\langle D_1^{m+1} \rangle$ for a layer reaches a specified critical damage, D_{cr}, then it set to D_{max}. The other two principal values $\langle D_2^{m+1} \rangle$ and $\langle D_3^{m+1} \rangle$ are also updated in a similar manner to Equation (13) as $\langle D_2^{m+1} \rangle = \langle D_3^{m+1} \rangle = (1-\gamma) \langle D_{max} \rangle$, unless this update reduces their values. Previously, published values of D_{cr} for ice range from $D_{cr}=0.45$ (Duddu & Waisman, 2012) to 0.6 (Duddu & Waisman, 2013), and we set D_{cr} to 0.6 throughout this paper. Note that not all damage tensors on all layers of a material point are guaranteed to have the same orientation. Misalignments with depth can occur as damage initiates at different times and accumulates under varying stress fields over time. However, misalignment is minimal in the simulations presented here.

3.6. 2-D damage update and rift treatment

After the 3-D damage update, the vertically-averaged damage that will be implemented into the SSA, $\overline{D}^{m+1}$, is calculated according to (21). As was done for 3-D damage, a 2-D brittle rupture condition can be set by defining a vertically-averaged critical damage, $\overline{D}_{cr}$, and maximum damage, $\overline{D}_{max}$. However, upon brittle rupture in 2-D, we set all components of $\overline{D}$ to $\overline{D}_{max}$ rather than only the maximum principal component as in the 3-D case. This 2-D treatment is consistent with complete failure of the material point, or the formation of a rift. Larger values of $\overline{D}_{max}$ are associated with a faster rate of rift widening and greater downstream velocities, and we find values for $\overline{D}_{max}$ of approximately 0.85—0.9 produce well-controlled and distinct rifts for the simulations presented here. Physically, setting a value of $\overline{D}_{max}$ less than unity can be interpreted as allowing some residual strength between the flanks of the rift, which can occur when rifts contain ice mélange that is structurally coherent enough to transmit stresses (Rignot & MacAyeal, 1998; Larour et al., 2004; Borstad et al., 2013). A complete description of rift forces should include a boundary condition on the rift flank walls similar to at the ice front (4), but which can also account for the pressure of ice mélange (Larour et al., 2014). This boundary condition acts to oppose rift opening. For simplicity, we do not explicitly implement such a boundary condition here; rather, its effect on the rift opening rate is implicitly accounted for by setting the value of $\overline{D}_{max}$ lower than unity. We discuss the potential for implementing more complex rift dynamics, including a rift wall boundary scheme, within the damage and GIMPM-SSA framework in Section 5.

3.7. SSA solution and material point updates

Damage is incorporated into the SSA solution by replacing $\dot{\varepsilon}$ in (2) with $\tilde{\dot{\varepsilon}}$, which is calculated from (7) using $\overline{D}$ as the damage variable. This substitution modifies the original SSA-GIMPM discretization (see Huth et al., 2020), yielding the following element sub-matrices of the tangent matrix, K, that are computed by summing over material points:

$$K_{11IJ} := \sum_{p=1}^{n_p} A_p \overline{\eta}_p H_p \text{¿}$$

$$+\frac{\partial S_{Jp}}{\partial x_2}\left[\frac{1}{2}\frac{\partial \phi_{Ip}}{\partial x_2}\left(2-D_{11}-D_{22}\right)-\frac{\partial \phi_{Ip}}{\partial x_1}D_{12}\right]\Bigg\}+\sum_{p=1}^{n_p} A_p \hat{\beta}_p \phi_{Ip} S_{Jp}, \tag{24}$$

$$K_{22IJ} := \sum_{p=1}^{n_p} A_p \bar{\eta}_p H_p ¿$$
$$¿$$

$$K_{12IJ} := \sum_{p=1}^{n_p} A_p \bar{\eta}_p H_p ¿$$
$$¿$$

$$K_{21IJ} := \sum_{p=1}^{n_p} A_p \bar{\eta}_p H_p ¿$$
$$+¿$$

In (24), material point parameters are indicated with the subscript p, where A_p is the material point area,$\hat{\beta}_p$ is the friction parameter, and n_p is the number of material points in the element. Nodal indices are indicated with I and J. We adopt the same shorthand from Part I (Huth et al., 2020) to notate the evaluation of the linear (ϕ_{Ip}¿ and GIMPM (S_{Jp}) shape functions at a material point, where $\phi_{Ip} = \phi_I(x_p)$ and $S_{Jp} = S_J(x_p)$. After the SSA is solved, the computational cycle for the GIMPM then continues as described in Part I (Huth et al., 2020), where the grid solution is used to update material point velocity, 2-D position, areal domain, and thickness. We use the algorithm XPIC(*k*) (eXtended Particle In Cell of order *k*) to perform the velocity and position updates, an algorithm that eliminates potential noise or overdamping associated with simpler update schemes (Hammerquist & Nairn, 2017). In agreement with a previous damage study (Nairn et al., 2017), we find that taking *k* = 5 yields sharp and stable crack propagation. Because each layer of a material point has the same horizontal velocity, updating the 2-D position of the material points automatically accounts for advection of any 3-D field, such as damage. Therefore, 3-D advection is essentially computationally free in the GIMPM-SSA framework. Conversely, using mesh-based Eulerian methods for advection would require solving a 2-D equation for each layer, or a single 3-D equation for the whole system. These Eulerian approaches would be much more expensive than the GIMPM-SSA framework, especially given our use of a tensorial damage variable; in addition, Eulerian advection schemes would suffer from artificial numerical diffusion.

4. Idealized test case: MISMIP+

We carry out three experiments to test the SSA creep damage model under different tunings and compare its performance to previously-published SSA damage models. We begin each experiment from the undamaged steady state configuration from the Marine Ice Sheet Model Intercomparison Project (MISMIP+, Asay-Davis et al., 2016), and allow damage and ice flow to evolve over time. In Section 4.1, we describe the MISMIP+ model setup. In Section 4.2, we show how the creep damage model can initiate a realistic damage field, which subsequently evolves to propagate rifts resulting in tabular calving. We perform sensitivity tests for the anisotropy parameter, mesh resolution, the nonlocal length scale, and the impact of an isothermal versus linear temperature profile. The creep damage model ultimately captures physically-consistent and numerically-stable rifting that previous crevasse-tracking SSA damage approaches are not well suited for replicating. For comparison, we test a crevasse-tracking damage model (Sun et al., 2017) in Section 4.3. where crevasse depths are calculated using the “zero-stress” criterion (Nye, 1957). We conduct further tests with the zero-stress damage model in Section 4.4, but where we modify the model to also account for the effects on damage from necking and mass balance (Bassis & Ma, 2015).

4.1. MISMIP+

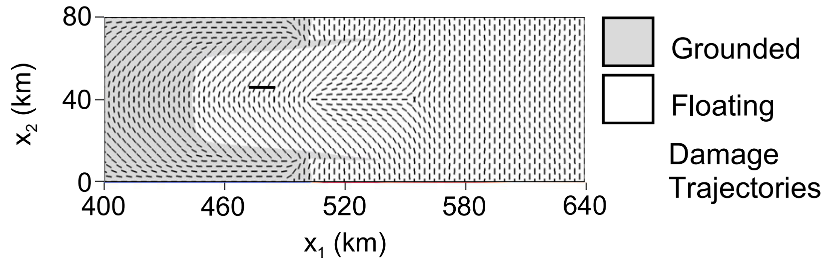

Figure 1. The MISMIP+ steady-state grounding line configuration and initial anisotropic damage trajectories. The trajectories correspond to the plane along which accumulates, and can be interpreted as crevasse patterns.

The MISMIP+ geometry is rectangular. In the longitudinal direction, the domain spans from an ice divide at $x_1 = 0$ km to an ice front at $x_1 = 640$ km. We do not allow the position of this ice front to evolve over time. The lateral boundaries span from $x_2 = 0$ km to $x_2 = 80$ km, and the entire system has a plane of symmetry about $x_2 = 40$ km. Normal velocities are set to zero (i.e. zero inflow) at all boundaries except at the ice front, where the Neumann boundary condition (4) is applied. The bedrock topography is a U-shaped submarine trough. Detail of the steady-state grounding configuration is shown in the grey shading of Figure 1. At the most retreated section of the steady-state grounding line (x_1 450 km), the bed has a retrograde slope. The higher sidewalls of the bedrock trough result in thin protrusions of laterally grounded ice that define the maximum longitudinal extent of the grounding line at x_1 537 km. All floating ice upstream of this point constitutes a laterally-supported shelf ice, whereas all ice downstream constitutes an unsupported floating ice tongue. The trajectories overlaying Figure 1 correspond to the 2nd principal component of anisotropic damage at the first time step, which may be interpreted as the initial development of crevasse patterns, or the plane along which $\langle \overline{D}_1 \rangle$ accumulates.

Starting from a thin slab of ice defined over the domain, we grew the system to steady state using the given MISMIP+ ice flow parameters and accumulation rate and a modified

Coulomb law for friction (Schoof, 2005; Gagliardini et al., 2007; Leguy et al., 2014). For this spin-up procedure, we use the SSA and thickness evolution solvers in the finite element software Elmer/Ice (Gagliardini et al., 2013). Without the damage model, the GIMPM-SSA model can hold the grounding line at its steady-state position for at least 100 years if no melt rate is assigned, satisfying the MISMIP+ Ice0 control experiment (Huth et al., 2020). Unless otherwise specified, we use a structured rectangular mesh/grid with a resolution of 0.5 km and initiate 9 regularly-spaced material points within each grid cell.

4.2. SSA creep damage simulations

We test our SSA creep damage model using the nonlocal integral formulation with the parameters given in Table 1, where , , and r, assume the values calibrated by Pralong and Funk (2005). We initially specify that the ice shelf is isothermal, so that the 3-D flow rate factor, B, does not vary with depth, and we set a stress threshold of $\sigma_{th}=0.12$ MPa. We set a nonlocal length scale of $l_c=1$ km, which roughly corresponds to the horizontal length of the fracture process zone, which we estimate from clusters of seismicity detected around a propagating rift on Amery Ice Shelf (Bassis et al., 2007). For our initial creep damage experiment, we test three different levels of damage anisotropy: $\gamma=0$, $\gamma=0.5$, and $\gamma=1$, which correspond to fully isotropic, evenly mixed isotropic/anisotropic, and fully anisotropic damage, respectively. Each simulation eventually results in tabular calving, at which point we end the simulation. We report results for the 2-D vertically-integrated maximum principal damage.

Initial damage accumulation: For all simulations, damage accumulation is minimal for interior grounded ice, where velocities and stresses are low due to basal friction. Downstream portions of the ice tongue also accumulate minimal damage, as strain-rates and stresses are low. Therefore, we only report results near t[...]ea[...]t. Figure 2 shows the early evolution of the princi[...]ot[...]pic case at (a) 0.06 years and (b) 0.2 years. At 0.06 y[...]at[...]along the ice shelf margins as expected, where stresses are large. However, the dominant damage accumulation occurs at x_1 520 km, where rifts initiate from the lateral boundaries of domain as indicated where $\langle \overline{D}_1 \rangle$= [...] ions, where they are tem[...]ion, and consequently, nearly identical damage patterns develop at similar rates for all values of γ tested (see Supplementary Figures S1a and S2a for the isotropic and mixed isotropic/anisotropic cases, respectively). Note that the lateral boundaries of the domain (x_2=0 km and x_2=80 km) can be considered symmetry boundaries because the normal velocities are set to zero, so that the rifts can be considered to have initiated from the center of small ice shelves. While rifts typically initiate at grounded margins, rift initiation from the center of ice shelves has occurred, for example, at Pine Island Glacier (Jeong et al., 2016).

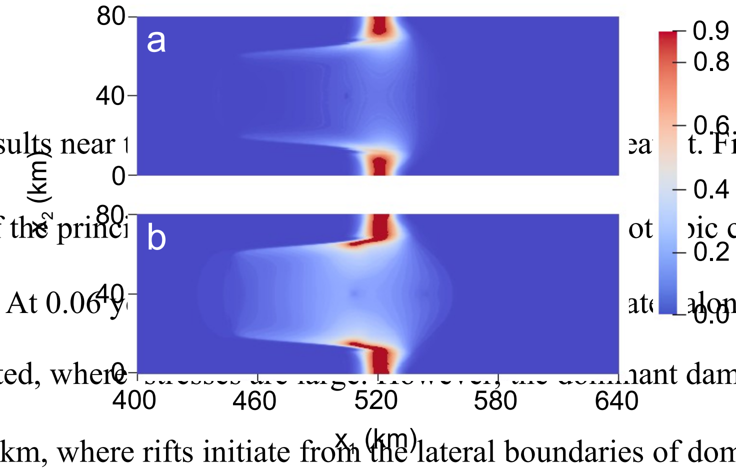

Figure 2. Maximum principal damage field for the fully anisotropic () creep damage simulation at **(a)** 0.06 years and **(b)** 0.2 years. Material points with correspond to rifts.

The configuration in Figure 2a is maintained until the grounded lateral protrusions weaken and thin enough to allow the rifts to propagate through ~0.1 years later, at which point these regions also unground. The rifts propagate upstream following the elevated damage that previously developed along the ice shelf margins, as shown in Figure 2b at 0.2 years. As in Figure 2a, rifts for the lower-anisotropy cases also propagate into a similar configuration, but now the rates of propagation are faster for lesser anisotropy. A comparable rift configuration develops in the fully-isotropic case by ~0.12 years and in the mixed isotropic/anisotropic case by ~0.18 years (Figures S1b and S2b).

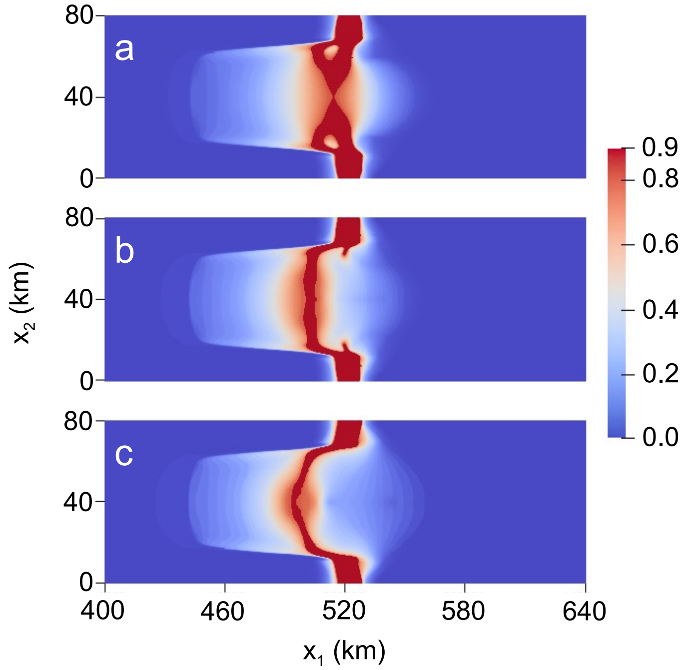

Figure 3. Maximum principal creep damage field at calving for: **(a)** isotropic); **(b)** mixed isotropic-anisotropic (; **(c)** fully anisotropic (damage. The corresponding times to calving are **(a)** 0.165 years; **(b)** 0.272 years; **(c)** 0.486 years.

Tabular calving: The rifting pattern in Figure 2b represents the final configuration before rifts propagate laterally across the domain to result in tabular calving. It is also the last configuration in which the spatial distribution of damage is similar for all values of γ. Figure 3 gives the final depth-averaged principal damage field $\langle \overline{D}_1 \rangle$ at calving. For the isotropic case (Figure 3a), the original rifts branch so that two points of calving occur; one branch originating from the upstream point of rifting reached in Figure S1b, and the other originating from a downstream position lateral to where the rift initiated at $x_1 \sim 520$ km. This second branch also partially develops for the $\gamma = 0.5$ case. However, for both the mixed isotropic/anisotropic (Figure 3b) and fully-anisotropic (Figure 3c) cases, calving ultimately stems from the further upstream location.

Higher levels of anisotropy yield sharper and more arcuate rifts that are more characteristic of real ice shelves, and qualitatively, appear more "brittle" than results under lower anisotropy, which appear more “ductile”. Higher anisotropy is also associated with slower rates of rift propagation, where the fully-anisotropic case calves after 0.486 years versus 0.165 years for the isotropic case. However, we emphasize that it is the anisotropy, not the speed of propagation, that allows the sharper rift and additional features to be captured. Rerunning the isotropic damage simulation with the damage rate factor B^* that is 4 times smaller allows isotropic damage to evolve at a similar rate to the anisotropic case, but the damage pattern remains essentially unchanged. Similarly, lowering δ_2 so that less damage accumulates each time step has negligible effect. Lastly, we note that our choice of $\overline{D}_{cr}=$¿ 0.8 was arbitrary, and effectively eliminating the rupture criterion by setting $\overline{D}_{cr} = \overline{D}_{max}$ still allows the same rift patterns to develop, but with a smoother transition in damage between ruptured and unruptured ice (not shown). However, the jump in damage induced by setting $\overline{D}_{cr}$ lower than $\overline{D}_{max}$ yields more visually-distinct rifting, and is likely physically justified because highly-damaged shelf ice may experience vertical shear stresses not accounted for in the SSA (Bassis & Ma, 2015) that could contribute to full-thickness brittle rupture.

Interestingly, the anisotropy strongly impacted rift behavior despite our simple scheme of representing rifts by setting all damage components of failed material points to $\overline{D}_{max}$. As the rift is represented by isotropic damage under our current treatment, it is the sub-critical damage that is controlling the rift path. The damage trajectories in Figure 1 show a clear arcuate pattern on the ice shelf that spans the lateral grounded margins, where the commonly observed pattern of en-échelon crevassing is reproduced. Rift propagation more closely follows these trajectories with higher levels of damage anisotropy.

Sensitivity to nonlocal damage length scale: The choice of the nonlocal length, l_c, is important in determining the computational cost of simulations, because a larger l_c allows larger element sizes to be used without grid bias. Ideally, l_c should be three or four times the element size to guarantee that mesh depend… 1k… which is twice the element size, appears to be s… bl… l_c to 2 km and rerunning the fully-anisotropic case yi… ng… Figure 4a) as the 1 km case (Figure 3c). To further … te… we rerun this l_c = 2 km fully-anisotropic case with 1 … ft path and time to calving is realized (Figure 4b). The largest difference between simulations using l_c = 2 km and l_c = 1 km is th… Fi… ur cr… an… e m…

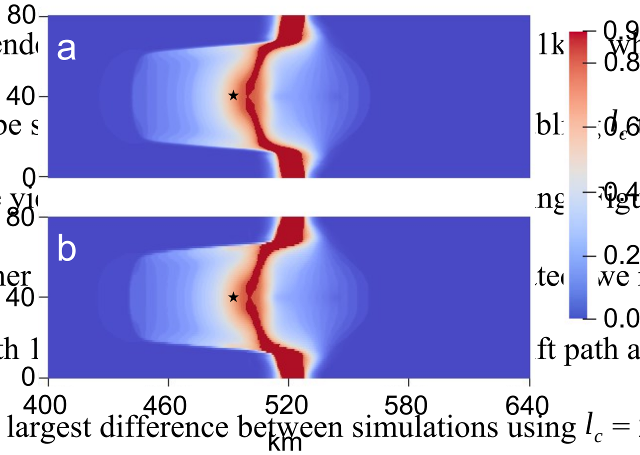

Figure 4. Maximum principal creep damage field at calving for fully anisotropic case (when using a nonlocal length scale = 2 km and **(a)** 0.5 km versus **(b)** 1 km grid resolution. Alleviation of grid dependence is evident in the similarity of damage patterns between the two simulations, as well as the comparable times to calving of **(a)** 0.493 and **(b)** 0.510 years. These rift patterns and calving times are also similar to those in Figure 3c, which uses a 0.5 km grid and = 1 km. The most apparent difference is that rifting in the the = 1 km case penetrates slightly farther upstream, as marked by the stars.

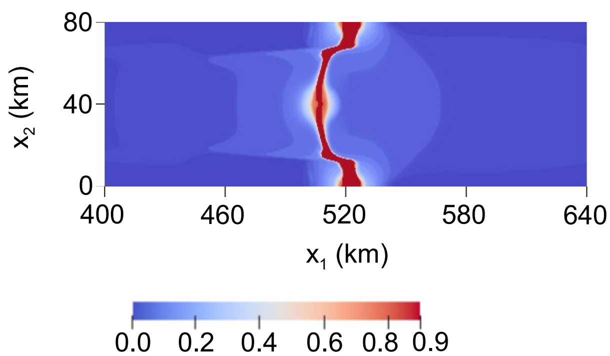

Figure 5. Maximum principal damage field at calving for fully anisotropic (creep damage when using the linear temperature profile and = 1 km.

insensitivity to l_c likely obviates the need for these more complex nonlocal schemes.

Effect of temperature gradient: Our final test with the creep damage model highlights how vertically-varying temperature can influence damage evolution. In this test, we assign a linear vertical temperature profile for each material point, where the ice base temperature is set to -2 ˚C, and the surface temperature is set to the value that yields the same depth-averaged rate factor, $\overline{B}$, from the isothermal case (approximately −¿16.7˚C). To allow direct comparison with Figure 3c, we set l_c=1 km. The maximum principal damage field at calving corresponding to this temperature profile is given in Figure 5. Due to the warmer basal temperature, basal crevasses only propagate in the most stressed regions and the overall damage field is reduced outside of the rift. This reduced basal calving is likely more consistent with reality, where basal crevasses should only initiate from the center of the shelf under very high stresses. More commonly, flexural stresses, such as those experienced at the grounding line, are required to initiate basal crevasses (Logan et al., 2013), which we discuss further in Section 5. The ease with which temperature effects can be accounted for is an advantage of the GIMPM-SSA creep damage model. Conversely, the zero-stress model employed in the next two sets of experiments is formulated under the assumption of an isothermal ice shelf, and therefore always overestimates the spatial extent of basal crevassing.

4.3. Zero-stress damage simulations

The zero-stress criterion (Nye, 1957), states that closely-spaced field of crevasses propagate to depths where the net longitudinal maximum principal Cauchy stress becomes zero. A previous study defined a zero-stress damage variable as the ratio of the combined depths of surface and basal crevasses to the ice thickness (Sun et al., 2017). This previous study only considered isotropic damage, but here, we extend the zero-stress damage variable to anisotropic form as a 2nd order tensor, $\widehat{D}$. We detail the anisotropic zero-stress damage model and its implementation in Supplementary Material S.2. To summarize, the zero-stress model calculates 3-D stresses using a similar effective pressure as Equations (15)-(17) used in the creep damage model, and ignoring the water pressure term for surface crevasses. However, the zero-stress damage model is formulated in terms of *applied* stress and under the assumption that crevasses are closely-spaced and in equilibrium with the stress field, where deviatoric stresses are considered depth-invariant here. Conversely, the creep damage model is updated in rate form according to depth-varying *effective* deviatoric stresses and a parameterized pressure, both of which are sensitive to depth-varying temperature and damage. Put simply, the zero-stress model parameterizes crevasse depths only, while the creep damage function is a dynamic parameterization of the actual fracture process at each depth. A vertical damage profile for a column of ice according to the zero-stress model resembles a step function, with maximum damage at depths where crevasses have propagated and zero damage elsewhere. Conversely, a typical vertical profile using creep damage exhibits sub-critical damage accumulation, because creep damage parameterizes the progressive accumulation of microcracks.

Here, we test the zero-stress damage model on the MISMIP+ domain to demonstrate the impact of these differences in comparison to the creep damage results from Section 4.2. We run two experiments with the zero-stress damage model, where each experiment tests the model in both fully-isotropic and fully-anisotropic form. Note that we ignore mass balance entirely for both ice flow and its influence on damage until Section 4.4 when we test the modification proposed by Bassis and Ma (2015).

In the first experiment, we run the zero-stress damage model as given for 30 years to show that the zero-stress assumptions alone are insufficient to initiate rifting. No critical rupture scheme is enforced. Note that in isotropic form, this test has been performed previously on a longer timescale using the MISMIP+ geometry with the finite volume ice flow model BISICLES (Sun et al., 2017). The isotropic zero-stress damage results near the grounding line are shown in Figure 6 at (a) 0 years, (b) 16 years, and (c) 30 years. At the first time step, damage immediately grows to $\widehat{D}$ 0.33 near the grounding line and $\widehat{D}$ 0.5 at the center of the ice shelf. With the

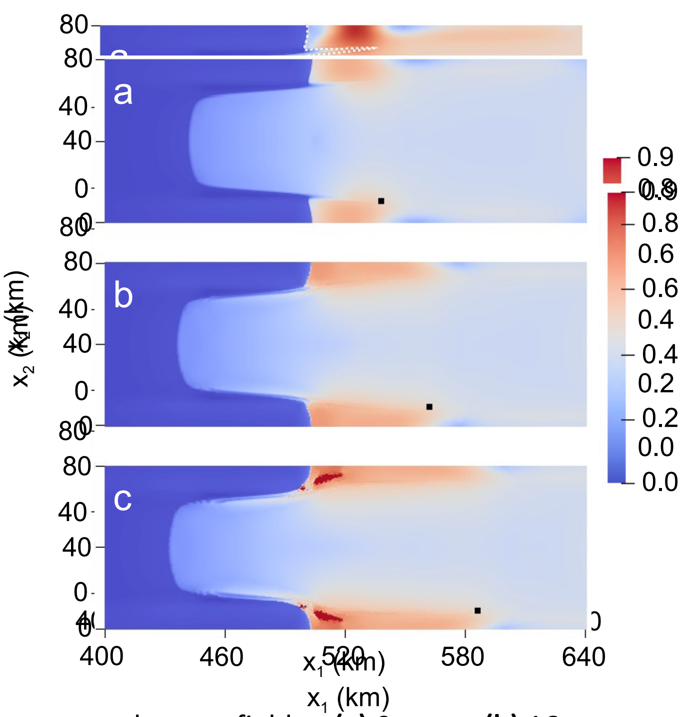

Figure 6. Isotropic zero-stress damage field at **(a)** 0 years, **(b)** 16 years, and **(c)** 30 years. The

Figure 7. Fully anisotropic zero-stress maximum principal damage field at **(a)** 0 years, **(b)** 16 years, and **(c)** 30 years. The black tracer particle highlights the highly-advective flow regime.

exception of rifting, the zero-stress and creep damage models generally agree concerning the spatial distribution of heavily versus weakly damaged areas. As was the case for creep damage, grounded ice experiences relatively little damage, as the effective pressure is dominated by the contribution from ice overburden pressure. Nearly ruptured ice immediately develops between the narrow strip of grounded ice at approximately x_1 520 km and the lateral boundaries ($x_2=$¿ 0 and $x_2=$¿ 80 km). However, this region does not develop into a sharp rift that propagates across the shelf to result in a calving event. Over time, the zero-stress damage field mostly evolves from its initial configuration through advection, as evident following the black tracer particle in Figures 6a and 6b, which advects beyond the domain in Figure 6c. As expected, the damage field has a strong impact on the grounding line position (white dotted line) by decreasing buttressing to initiate grounding line retreat. This grounding line migration is reflected in the damage field, as ice that is nearing floatation quickly accumulates relatively heavy damage in comparison to upstream grounded ice. The corresponding anisotropic zero-stress damage results are given in Figure 7, which yield lesser damage values everywhere compared to the isotropic case given that damage accumulation is restricted to a single plane. Like the isotropic case, damage evolution is largely dictated by advection, though relatively less advection occurs over the 30-year simulation, as indicated by the black tracer particle, because the lesser damage results in smaller velocities. While some material points eventually rupture by the end of the simulation, they do not result in tabular calving, even if the simulation is continued for several more decades. In agreement with Sun et al. (2017) none of the above zero-stress simulations resulted in calving. We can conclude that the novelties of our approach, namely using a tensorial damage variable and implementing the model within the GIMPM-SSA framework, are simply not enough to cause calving with the zero-stress model in the MISMIP+ experiment.

In the second zero-stress damage experiment, we rerun the MISMIP+ experiment, but encourage rifting to initiate by setting critical damage values of $\widehat{D}_{cr}=0.7$ and $\widehat{D}_{cr}=0.6$ for

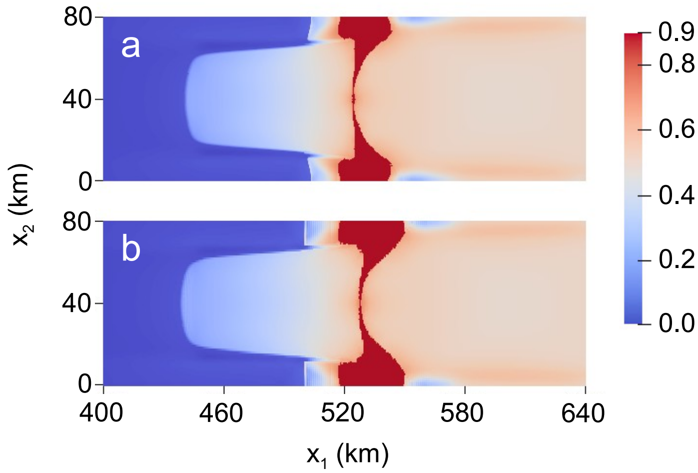

Figure 8. Isotropic zero-stress damage field at calving when using = 0.7 for a grid resolution of **(a)** 0.5 km versus **(b)** 1 km. Grid dependence is most apparent in the vastly different times to calving of **(a)** 0.553 years versus **(b)** 1.607 years.

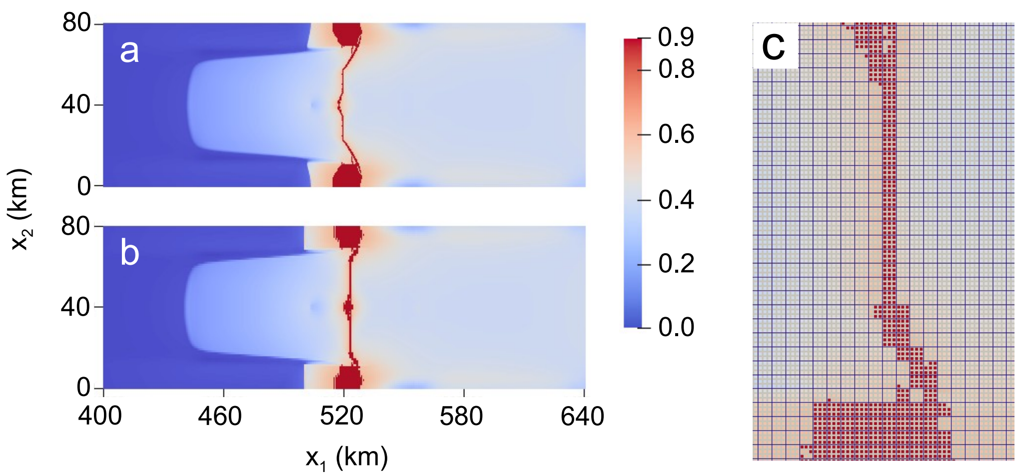

Figure 9. Fully anisotropic zero-stress maximum principal damage field at calving when using = 0.6 for a grid resolution of **(a)** 0.5 km versus **(b)** 1 km. The rifts propagate nearly instantly, with times to calving of **(a)** 5.73 hours and **(b)** 5.99 hours. The rift paths show clear grid dependence, as shown in detail **(c)** for the 1 km case.

isotropic and anisotropic damage, respectively. The critical rupture criterion is enforced after each combined zero-stress damage and SSA solution. At the first time step, rupture occurs near the shear margins where $\langle \hat{D}_1 \rangle > \hat{D}_{cr}$, and the resulting high stresses allow rifts to propagate across the domain to calve tabular icebergs. The final maximum principal zero-stress damage fields are given in Figures 8 and 9 for the isotropic and anisotropic cases, respectively. While both cases produce rifts in the same general area as the creep damage experiments, this experiment exposes several numerical and physical issues associated with zero-stress models that limit their general applicability for representing tabular calving. The primary numerical difficulty with this approach is that the zero-stress model is inherently a local damage model, and is therefore subject to grid dependence. Figures 8a and 9a use a 0.5 km grid resolution whereas Figures 8b and 9b use a 1 km grid resolution. Grid dependence in the isotropic case is only slightly apparent in the spatial damage field, but has a strong influence on the time to calving; the 0.5 km resolution grid results in calving in 0.553 years versus 1.607 years for the 1 km resolution grid. Stronger grid dependence is observed in the spatial damage field for the anisotropic case. The differing grid resolution results in different rift paths, where damage clearly localizes to single grid cells, as shown in detail for the 1 km resolution case in Figure 9c.

In general, using the zero-stress damage model to simulate rift propagation is problematic due to the assumption that crevasse depths are in equilibrium with the stress field instead of using a rate-based parameterization of fracture as in the creep damage model. The rate-based parameterization allows more precise tuning of the rates of damage accumulation and rift propagation by varying the parameter $B^{¿}$ in the creep damage evolution function (9). Furthermore, creep damage will preferentially accumulate faster wherever the magnitudes of the Hayhurst stress, χ, and previous damage are greatest. Conversely, the zero-stress damage rate cannot be controlled, which was particularly problematic during the anisotropic critical rupture test, where calving occurred in under 6 hours for both grid resolutions. The corresponding timestep sizes were as small as fractions of a second in an attempt to keep $\overline{dD}_{max}$ less than 0.075

according to the time-stepping scheme, a restriction that was not always satisfied. In practice, such miniscule time steps are only sustainable for modeling nearly-instantaneous calving. Therefore, a lack of tuning controls can be added to the many issues associated with using zero-stress damage for Antarctic ice shelves, along with the potential physical-inconsistencies concerning assumptions on crevasse spacing and vertically-invariant deviatoric stresses, as well as grid-dependence due to the local damage formulation. Based on these studies, we conclude that the zero-stress damage model is not well suited for parametrizing ice shelf fracture, except where crevasses are closely spaced and damage is small enough that localization and full-thickness rifting do not occur. Under the assumption that vertical temperature profiles are isothermal, the zero-stress model will typically overestimate basal crevasses. Furthermore, rifts are poorly represented in the zero-stress model, if they are initiated at all.

4.4. Simulations using the modification for necking and mass balance

A drawback of both the creep and zero-stress damage models as tested above is that they do not account for the potential impact that processes associated with necking and mass balance may have on damage evolution. In Supplementary Material S.3, we explain how these processes influence crevasse depths, and we describe an expression that modifies large-scale damage to account for these processes (Bassis & Ma, 2015). In this section, we implement this expression within the zero-stress damage model, noting that implementation within the creep damage model is much more complex and is beyond the scope of this paper. By comparing the results from this modified zero-stress damage model to those of the previous unmodified version, we can analyze how necking and mass balance processes impact damage. Thus, we can determine the settings in which our creep damage model is applicable in its current form without accounting for these processes, and then propose how a combined approach between damage models may be formulated for more generalized applications.

We perform two experiments with the modified zero-stress model. Both experiments

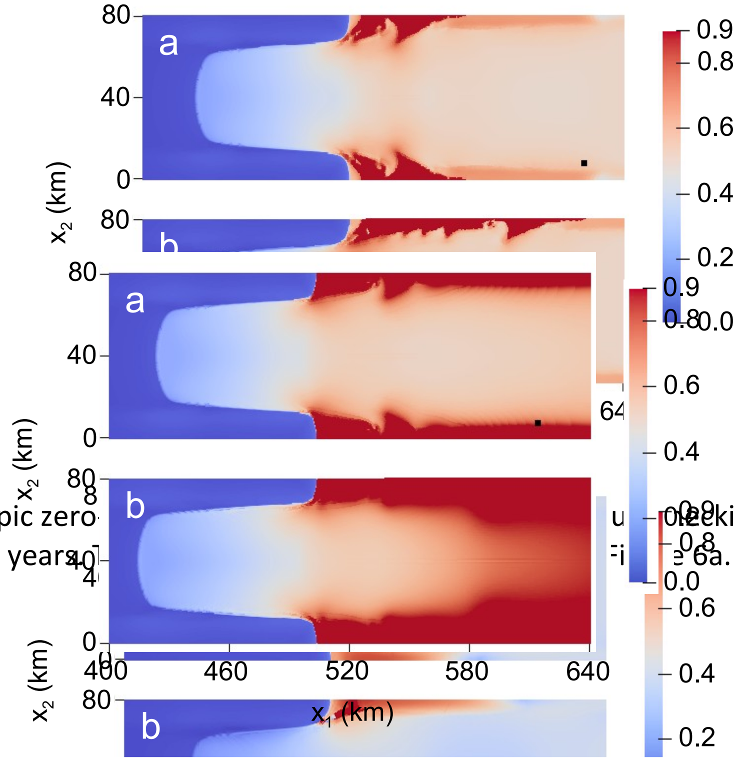

Figure 10. Isotropic zero ... necking, at **(a)** 16 years, and **(b)** 30 years ... 6a.

Figure 12. Isotropic zero-stress damage field, as modified to include necking and 5 m a^{-1} basal melting for floating ice, at **(a)** 16 years, and **(b)** 30 years. The initial field at 0 years is identical to Figure 6a.

Figure 11. Fully anisotropic ... d, as modified to include necking, at **(a)** 16 ... ears is identical to Figure 7a.

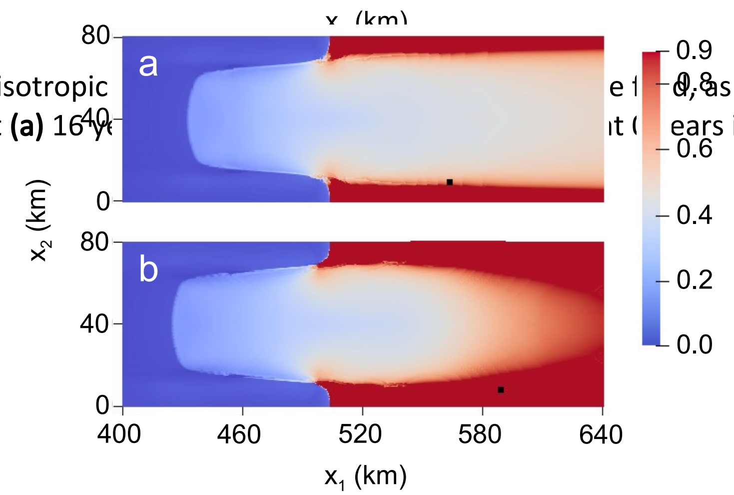

Figure 13. Fully-anisotropic zero-stress maximum principal damage field, as modified to include necking and 5 m a^{-1} basal melting for floating ice, at **(a)** 16 years, and **(b)** 30 years. The initial field at 0 years is identical to Figure 7a.

resemble the first experiment from the previous section, where the damage model is activated and the MISMIP+ model is run forward in isotropic and anisotropic form for 30 years. For the first experiment, we set mass balance to zero, so that when the modified and unmodified zero-stress damage results are compared, the role of necking processes alone are revealed. The results for the necking-only experiment are shown in Figures 10 and 11 for the isotropic and anisotropic cases, respectively. The first timestep is not shown because it is the same as the unmodified case (Figure 6a). Like the unmodified case, the necking model gives high values of damage near the margins, where the greatest damage is concentrated at x_1 520 km. These areas are associated with high stresses and $S_0 < 1$, so that necking accelerates the rate of damage accumulation, though rifts still do not propagate across the center of the shelf. However, the rifting in the modified isotropic case develops into much sharper patterns than in the unmodified isotropic case, which is not only due to the accelerated damage accumulation in these areas, but also due to healing in the immediate surrounding areas ($S_0 > 1$). Elevated damage values in these areas are also observable in the anisotropic modified case, relative to the anisotropic unmodified case. As predicted in Bassis and Ma (2015), the necking expression only yields additional damage accumulation along these areas of elevated shear, with healing dominating the response elsewhere. However, upon healing, most regions of the domain quickly re-damage towards their previous values. For example, the ice tongue part of the domain is largely under uniaxial tension, which in the isotropic case, yields the expected values of $\widehat{D} \approx 0.5$ and $S_0 \approx 2$. Any healing from the necking model is immediately countered by new zero-stress damage accumulation during the next computational cycle. However, at the location where the ice tongue in the unmodified case inherits heavy damage from upstream along the lateral bounds (Figures 6b and 6c), healing is observed in the modified case that is maintained over time (Figure 10). In the anisotropic case (Figure 11), sustained healing is more apparent along the shear margins of the ice shelf.

For the modified zero-stress second experiment, we test the impact of assigning a basal melt rate. We rerun the first experiment with a basal melting rate of 5 m a^{-1}, which is taken as constant throughout the floating ice domain, for simplicity. The isotropic and anisotropic results are given in Figures 12 and 13, respectively, and we note that setting a greater or lesser basal melting rate yields similar patterns. For the isotropic case, the damage field at 16 years (Figure 12a) is very similar to the necking-only case (Figure 10b) everywhere except near the lateral bounds of the floating domain, because basal melting is not strong enough to offset the effect of healing. The opposite affect occurs near the lateral bounds of the floating domain, and maximum damage is quickly realized. By the end of the simulation (Figure 12b), the ice shelf has thinned enough that melting begins to dominate over healing for more interior sections of the ice tongue. The same response is observed in the anisotropic case (Figure 13), except that at the interior sections of the ice tongue, melt-induced damage slightly overtakes healing earlier in the simulation than the isotropic case. Healing is this area is lower for the anisotropic case than the isotropic case, because damage, and therefore strain-rates, are lower.

5. Discussion

The experiments from Section 4.4 indicate that necking and mass balance may play significant roles in modulating damage on decadal timescales, so that these processes should be implemented within the creep damage model if it is to be applied on long timescales. Such an approach will be the subject of future research, and would require carefully modifying the 3-D damage field to reflect the modified value of vertically-integrated damage calculated according to necking and mass balance. This process could include adjusting the vertical coordinates and local damage values of each layer, as well as the addition or subtraction of layers. Based on our previous comparison between creep damage and zero-stress damage, we would expect a combined creep-damage/necking model to behave somewhat differently than the combined zero-stress damage/necking model. While incorporating necking effects simply sharpened the zero-stress damage field in regions of elevated stress, this sharpened damage could develop into rifting with the creep damage model that would otherwise not occur. Similarly, targeted basal melting could also trigger additional rifting. However, we emphasize that necking and mass balance effect should not be always be necessary to initiate rifts. Encouragingly, the creep damage model can initiate realistic rifting without these additional effects (Section 4.2), though we acknowledge that given the idealized setting, it is difficult to determine whether or not this rifting should actually occur. Potentially, necking could play a more apparent role in small scale calving at the ice front; qualitatively, the configuration of fully-damaged material points in the isotropic modified zero stress simulation (Figure 10b) resembles the sawtooth pattern of calving sometimes observed at the lateral sides of long ice tongues (e.g. Erebus ice tongue).

The major advantage of combining the Bassis and Ma (2005) model with creep damage concerns healing. Basal crevasses are typically initiated near the grounding line or perturbations such as ice rises, and can heal heavily as they advect downstream, due to both necking and marine ice formation. Healing of upstream damage has been inferred, for example, on Larsen C Ice Shelf (Borstad et al., 2013). Healing in the modified zero-stress experiments was probably underestimated; most healing was immediately offset by new damage because the zero-stress model assumes crevasse depths are in equilibrium with the stress field, and zero-stress deviatoric stresses were assumed depth-invariant here so that basal crevassing was likely overestimated. However, creep damage is rate-based and can incorporate 3-D temperature and stresses. As seen in Figure 5, when lower basal temperatures are accounted for, basal crevasses do not spontaneously propagate in low stress regions at the interior of the ice shelf. Therefore, when using a combined creep-damage/necking model with mass balance effects, damage associated with deep basal crevasses that were initiated from high stress regions upstream could become completely healed in low stress regions downstream. However, the success of capturing this behavior is reliant on proper initiation of the damage field corresponding to upstream basal crevasses. In the case that basal crevasses initiate from flexural stresses at the grounding line, special treatment is required to initiate the corresponding damage because such stresses are not captured in the SSA. The simplest approach may be to assign a 3-D damage distribution according to crevasse depths calculated with the SSA zero-stress approximation. However, this approach would be strictly a rough approximation, as for example, the zero-stress model was found to significantly underestimate basal crevasse depths near the grounding line on Larsen C Ice Shelf where flexural stresses are large (Luckman et al., 2012). These authors found better agreement with observations (within 10-20%) when using a linear elastic fracture mechanics approach, though this approach also did not explicitly account for flexural stresses and may not be accurate in all cases. An approach for approximating basal crevasse depth at the grounding line that does account for flexure involves using a thin elastic beam approximation, combined with a mode I brittle failure criterion (Logan et al., 2012), but this model is only applicable where strain rates are low. The most accurate way of capturing flexural stresses may be to transition to a full-Stokes model near the grounding line, though this approach is extremely computationally expensive in 3-D. Linear elastic fracture mechanics has been used to obtain reasonable basal crevasse heights in a 2-D full-Stokes setting (Yu et al., 2017), or the creep damage model could potentially be applied.

One of the most significant advancements made with the creep damage framework presented here is in modeling the initiation and propagation of rifts using damage. While it is encouraging that our simple isotropic rift treatment cleanly propagates rifts, our ongoing research efforts are aimed at enabling a more accurate physical depiction of rift dynamics. Ideally, wide rifts that open into the ocean should be implemented as a discontinuity, with a Neumann boundary condition assigned along the flanks similar to the ice front boundary condition, but which also includes the opposing pressure of ice mélange within the rift (Larour et al., 2014). Using material point methods, this boundary condition could potentially be applied directly on material points in a similar manner to how water pressure has been incorporated into full-Stokes creep damage simulations (Duddu et al., 2020). Alternatively, it could be applied along line segments that are introduced to track cracks, and which can advect with flow (Nairn, 2003). Once a discontinuous boundary treatment is implemented, behavior of ruptured material points can be further modified to account for the strength of mélange between flanks, tension/compression asymmetry, and lateral friction or faulting between flanks.

6. Conclusion

Mechanical weakening and fracture of large-scale ice shelves may be modeled using an SSA parameterization for nonlocal, anisotropic creep damage. Unlike previous crevasse depth-tracking damage approaches, creep damage parameterizes the fracture process itself, and is therefore better suited for capturing dynamic processes such as rifting. Furthermore, creep damage is treated in 3-D, which allows damage interaction with other 3-D variables, such as temperature and density. The numerical framework that we built to support the creep damage model is formulated on the material point method, which allows accurate and efficient advection of the 3-D damage field. In contrast, if the model was implemented within a traditional Eulerian framework, advection algorithms would be computationally inefficient, and introduce numerical diffusion error that would compromise the accuracy of damage evolution. By testing the creep damage model on an idealized marine ice sheet, we conclude that large scale damage of ice should be treated as highly anisotropic. Anisotropic creep damage yields sharper, more arcuate rifting and crevasse patterns that are more consistent with observations. In addition, anisotropic nonlocal damage is more thermodynamically consistent with the fracture physics (Pralong et al., 2006). Our experiments further show that deep crevassing, rifting, and tabular calving may occur using creep damage without the inclusion of necking or mass-balance processes. Testing a modified form of the zero-stress damage model that include these processes (Bassis & Ma, 2015) does not capture rifting that results in calving. Therefore, we conclude that the failure of zero-stress damage approaches to capture rifting does not occur due to the absence of these processes, but because the zero-stress model does not properly parameterize the fracture process and suffers from numerical issues related to its local formulation and assumption of equilibrium with the stress field. Future research should consider combining the necking/mass-balance and creep damage models for an ideal representation of ice-shelf fracture on decadal timescales. Ongoing research will also focus on verification of the damage parameters, application to real ice shelves, and improved representation of rifting.

Acknowledgements

Huth was funded by NASA Earth and Space Sciences fellowship under grant no. NNX15AN99H. Duddu gratefully acknowledges the funding support provided by the National Science Foundation's Office of Polar Programs via CAREER grant \#PLR-1847173. Smith was funded under the NASA grant no. NNX13AP69G.

References

Albrecht, T., & Levermann, A. (2014). Fracture-induced softening for large-scale ice dynamics. *Cryosphere, 8*(2), 587-605. doi:10.5194/tc-8-587-2014

Albrecht, T., Martin, M., Haseloff, M., Winkelmann, R., & Levermann, A. (2011). Parameterization for subgrid-scale motion of ice-shelf calving fronts. *Cryosphere, 5*(1), 35-44. doi:10.5194/tc-5-35-2011

Alley, R. B., Horgan, H. J., Joughin, I., Cuffey, K. M., Dupont, T. K., Parizek, B. R., . . . Bassis, J. (2008). A Simple Law for Ice-Shelf Calving. *Science, 322*(5906), 1344-1344. doi:10.1126/science.1162543

Asay-Davis, X. S., Cornford, S. L., Durand, G., Galton-Fenzi, B. K., Gladstone, R. M., Gudmundsson, G. H., . . . Seroussi, H. (2016). Experimental design for three interrelated marine ice sheet and ocean model intercomparison projects: MISMIP v. 3 (MISMIP+), ISOMIP v. 2 (ISOMIP+) and MISOMIP v. 1 (MISOMIP1). *Geoscientific Model Development, 9*(7), 2471-2497. doi:10.5194/gmd-9-2471-2016

Bardenhagen, S. G., & Kober, E. M. (2004). The generalized interpolation material point method. *Cmes-Computer Modeling in Engineering & Sciences, 5*(6), 477-495. doi:10.3970/cmes.2004.005.477

Bassis, J. N., Fricker, H. A., Coleman, R., Bock, Y., Behrens, J., Darnell, D., . . . Minster, J.-B. (2007). Seismicity and deformation associated with ice-shelf rift propagation. *Journal of Glaciology, 53*(183), 523-536. doi:10.3189/002214307784409207

Bassis, J. N., Fricker, H. A., Coleman, R., & Minster, J.-B. (2008). An investigation into the forces that drive ice-shelf rift propagation on the Amery Ice Shelf, East Antarctica. *Journal of Glaciology, 54*(184), 17-27. doi:10.3189/002214308784409116

Bassis, J. N., & Ma, Y. (2015). Evolution of basal crevasses links ice shelf stability to ocean forcing. *Earth and Planetary Science Letters, 409*, 203-211. doi:10.1016/j.epsl.2014.11.003

Bassis, J. N., & Walker, C. (2012). Upper and lower limits on the stability of calving glaciers from the yield strength envelope of ice. *Proceedings of the Royal Society A: Mathematical, Physical and Engineering Sciences, 468*(2140), 913-931. doi:10.1098/rspa.2011.0422

Bazant, Z. P. (1986). Mechanics of distributed cracking. *Appl. Mech. Rev, 39*(5), 675-705. doi:10.1115/1.3143724

Borstad, C., Khazendar, A., Scheuchl, B., Morlighem, M., Larour, E., & Rignot, E. (2016). A constitutive framework for predicting weakening and reduced buttressing of ice shelves based on observations of the progressive deterioration of the remnant Larsen B Ice Shelf. *Geophysical Research Letters, 43*(5), 2027-2035. doi:10.1002/2015gl067365

Borstad, C. P., Rignot, E., Mouginot, J., & Schodlok, M. P. (2013). Creep deformation and buttressing capacity of damaged ice shelves: theory and application to Larsen C ice shelf. *Cryosphere, 7*(6), 1931-1947. doi:10.5194/tc-7-1931-2013

Cougnon, E. A., Galton-Fenzi, B. K., Rintoul, S. R., Legrésy, B., Williams, G. D., Fraser, A. D., & Hunter, J. R. (2017). Regional Changes in Icescape Impact Shelf Circulation and Basal Melting. *Geophysical Research Letters, 44*(22), 11,519-511,527. doi:10.1002/2017gl074943

Depoorter, M. A., Bamber, J. L., Griggs, J. A., Lenaerts, J. T. M., Ligtenberg, S. R. M., van den Broeke, M. R., & Moholdt, G. (2013). Calving fluxes and basal melt rates of Antarctic ice shelves. *Nature, 502*(7469), 89-+. doi:10.1038/nature12567

Duddu, R., Bassis, J. N., & Waisman, H. (2013). A numerical investigation of surface crevasse propagation in glaciers using nonlocal continuum damage mechanics. *Geophysical Research Letters, 40*(12), 3064-3068. doi:10.1002/grl.50602

Duddu, R., Jiménez, S., & Bassis, J. (2020). A non-local continuum poro-damage mechanics model for hydrofracturing of surface crevasses in grounded glaciers. *Journal of Glaciology*, 1-15. doi:10.1017/jog.2020.16

Duddu, R., & Waisman, H. (2012). A temperature dependent creep damage model for polycrystalline ice. *Mechanics of Materials, 46*, 23-41. doi:10.1016/j.mechmat.2011.11.007

Duddu, R., & Waisman, H. (2013). A nonlocal continuum damage mechanics approach to simulation of creep fracture in ice sheets. *Computational Mechanics, 51*(6), 961-974. doi:10.1007/s00466-012-0778-7

Fürst, J. J., Durand, G., Gillet-Chaulet, F., Tavard, L., Rankl, M., Braun, M., & Gagliardini, O. (2016). The safety band of Antarctic ice shelves. *Nature Climate Change, 6*(5), 479. doi:10.1038/nclimate2912

Gagliardini, O., Cohen, D., Råback, P., & Zwinger, T. (2007). Finite-element modeling of subglacial cavities and related friction law. *Journal of Geophysical Research: Earth Surface, 112*(F2). doi:10.1029/2006JF000576

Ganczarski, A., & Skrzypek, J. (2001). Application of the Modified Murakami's Anisotropic Creep-Damage Model to 3D Rotationally-Symmetric Problem. *Technische Mechanik. Scientific Journal for Fundamentals and Applications of Engineering Mechanics, 21*(4), 251-260.

Giry, C., Dufour, F., & Mazars, J. (2011). Stress-based nonlocal damage model. *International Journal of Solids and Structures, 48*(25-26), 3431-3443. doi:10.1016/j.ijsolstr.2011.08.012

Glen, J. W. (1955). The creep of polycrystalline ice. *Proceedings of the Royal Society of London Series a-Mathematical and Physical Sciences, 228*(1175), 519-538. doi:10.1098/rspa.1955.0066

Hall, F. R., & Hayhurst, D. R. (1991). Modeling of grain-size effects in creep crack-growth using a nonlocal continuum damage approach. *Proceedings of the Royal Society-Mathematical and Physical Sciences, 433*(1888), 405-421. doi:10.1098/rspa.1991.0055

Hammerquist, C. C., & Nairn, J. A. (2017). A new method for material point method particle updates that reduces noise and enhances stability. *Computer Methods in Applied Mechanics and Engineering, 318*, 724-738. doi:10.1016/j.cma.2017.01.035

Hayhurst, D. (1972). Creep rupture under multi-axial states of stress. *Journal of the Mechanics and Physics of Solids, 20*(6), 381-382. doi:10.1016/0022-5096(72)90015-4

Huth, A., Duddu, R., Smith, B.E. (2020). A generalized interpolation material point method for shallow ice shelves. Part I: shallow shelf approximation and ice thickness evolution.

Jeong, S., Howat, I. M., & Bassis, J. N. (2016). Accelerated ice shelf rifting and retreat at Pine Island Glacier, West Antarctica. *Geophysical Research Letters, 43*(22), 11,720-711,725. doi:10.1002/2016gl071360

Jiménez, S., Duddu, R., & Bassis, J. (2017). An updated-Lagrangian damage mechanics formulation for modeling the creeping flow and fracture of ice sheets. *Computer Methods in Applied Mechanics and Engineering, 313*, 406-432. doi:https://doi.org/10.1016/j.cma.2016.09.034

Keller, A., & Hutter, K. (2014). Conceptual thoughts on continuum damage mechanics for shallow ice shelves. *Journal of Glaciology, 60*(222), 685-693. doi:10.3189/2014JoG14J010

Larour, E., Khazendar, A., Borstad, C., Seroussi, H., Morlighem, M., & Rignot, E. (2014). Representation of sharp rifts and faults mechanics in modeling ice shelf flow dynamics: Application to Brunt/Stancomb-Wills Ice Shelf, Antarctica. *Journal of Geophysical Research: Earth Surface, 119*(9), 1918-1935. doi:10.1002/2014JF003157

Larour, E., Rignot, E., & Aubry, D. (2004). Processes involved in the propagation of rifts near Hemmen ice rise, Ronne ice shelf, Antarctica. *Journal of Glaciology, 50*(170), 329-341. doi:10.3189/172756504781829837

Leguy, G. R., Asay-Davis, X. S., & Lipscomb, W. H. (2014). Parameterization of basal friction near grounding lines in a one-dimensional ice sheet model. *The Cryosphere, 8*(4), 1239-1259. doi:10.5194/tc-8-1239-2014

Lemaitre, J. (1971). *Evaluation of dissipation and damage in metals.* Paper presented at the Proc. ICM Kyoto.

Lemaitre, J. (2012). *A course on damage mechanics*: Springer Science & Business Media.

Lemaitre, J., & Chaboche, J. L. (1978). Phenomenological approach of damage rupture. *Journal De Mecanique Appliquee, 2*(3), 317-365.

Levermann, A., Albrecht, T., Winkelmann, R., Martin, M. A., Haseloff, M., & Joughin, I. (2012). Kinematic first-order calving law implies potential for abrupt ice-shelf retreat. *The Cryosphere, 6*, 273. doi:10.5194/tc-6-273-2012

Ling, X., Tu, S. T., & Gong, J. M. (2000). Application of Runge-Kutta-Merson algorithm for creep damage analysis. *International Journal of Pressure Vessels and Piping, 77*(5), 243-248. doi:10.1016/s0308-0161(00)00010-7

Liu, Y., Moore, J. C., Cheng, X., Gladstone, R. M., Bassis, J. N., Liu, H., . . . Hui, F. (2015). Ocean-driven thinning enhances iceberg calving and retreat of Antarctic ice shelves. *Proceedings of the National Academy of Sciences, 112*(11), 3263-3268. doi:10.1073/pnas.1415137112

Logan, L., Catania, G., Lavier, L., & Choi, E. (2013). A novel method for predicting fracture in floating ice. *Journal of Glaciology, 59*(216), 750-758. doi:10.3189/2013JoG12J210

Londono, Juan G., Berger-Vergiat, L., & Waisman, H. (2017). An equivalent stress-gradient regularization model for coupled damage-viscoelasticity. *Computer Methods in Applied Mechanics and Engineering, 322*, 137-166. doi:10.1016/j.cma.2017.04.010

Luckman, A., Jansen, D., Kulessa, B., King, E., Sammonds, P., & Benn, D. (2012). Basal crevasses in Larsen C Ice Shelf and implications for their global abundance. *The Cryosphere, 6*(1), 113-123. doi:10.5194/tc-6-113-2012

Macayeal, D. R. (1989). Large-scale ice flow over a viscous basal sediment - Theory and application to Ice Stream-B, Antarctica. *Journal of Geophysical Research-Solid Earth and Planets, 94*(B4), 4071-4087. doi:10.1029/JB094iB04p04071

MacGregor, J. A., Catania, G. A., Markowski, M. S., & Andrews, A. G. (2012). Widespread rifting and retreat of ice-shelf margins in the eastern Amundsen Sea Embayment between 1972 and 2011. *Journal of Glaciology, 58*(209), 458-466. doi:10.3189/2012JoG11J262

McGrath, D., Steffen, K., Scambos, T., Rajaram, H., Casassa, G., & Lagos, J. L. R. (2012). Basal crevasses and associated surface crevassing on the Larsen C ice shelf, Antarctica, and their role in ice-shelf instability. *Annals of glaciology, 53*(60), 10-18. doi:10.3189/2012AoG60A005

Mobasher, M. E., Duddu, R., Bassis, J. N., & Waisman, H. (2016). Modeling hydraulic fracture of glaciers using continuum damage mechanics. *Journal of Glaciology, 62*(234), 794-804. doi:10.1017/jog.2016.68

Morland, L. W., & Zainuddin, R. (1987). *Plane and Radial Ice-Shelf Flow with Prescribed Temperature Profile.* Paper presented at the A Workshop on the Dynamics of the West Antarctic Ice Sheet, Dordrecht.

Murakami, S., Ohno, N. (1980). *A continuum theory of creep and creep damage*. Paper presented at the 3rd Symposium Creep in Structures. International Union of Theoretical and Applied Mechanics, Leicaster, UK.

Murakami, S. (1983). Notion of Continuum Damage Mechanics and its Application to Anisotropic Creep Damage Theory. *Journal of Engineering Materials and Technology, 105*(2), 99-105. doi:10.1115/1.3225633

Murakami, S., Kawai, M., & Rong, H. (1988). Finite element analysis of creep crack growth by a local approach. *International Journal of Mechanical Sciences, 30*(7), 491-502. doi:10.1016/0020-7403(88)90003-3

Nairn, J. A. (2003). Material point method calculations with explicit cracks. *Computer Modeling in Engineering and Sciences, 4*(6), 649-664.

Nairn, J. A., Hammerquist, C. C., & Aimene, Y. E. (2017). Numerical implementation of anisotropic damage mechanics. *International Journal for Numerical Methods in Engineering, 112*(12), 1848-1868. doi:10.1002/nme.5585

Nick, F. M., Van Der Veen, C. J., Vieli, A., & Benn, D. I. (2010). A physically based calving model applied to marine outlet glaciers and implications for the glacier dynamics. *Journal of Glaciology, 56*(199), 781-794. doi:10.3189/002214310794457344

Nick, F. M., Vieli, A., Andersen, M. L., Joughin, I., Payne, A., Edwards, T. L., . . . van de Wal, R. S. W. (2013). Future sea-level rise from Greenland's main outlet glaciers in a warming climate. *Nature, 497*(7448), 235-238. doi:10.1038/nature12068

Nye, J. F., & Perutz, M. F. (1957). The distribution of stress and velocity in glaciers and ice-sheets. *Proceedings of the Royal Society of London. Series A. Mathematical and Physical Sciences, 239*(1216), 113-133. doi:10.1098/rspa.1957.0026

Paolo, F. S., Fricker, H. A., & Padman, L. (2015). Volume loss from Antarctic ice shelves is accelerating. *Science, 348*(6232), 327-331. doi:10.1126/science.aaa0940

Pollard, D., DeConto, R. M., & Alley, R. B. (2015). Potential Antarctic Ice Sheet retreat driven by hydrofracturing and ice cliff failure. *Earth and Planetary Science Letters, 412*, 112-121. doi:10.1016/j.epsl.2014.12.035

Pralong, A., & Funk, M. (2005). Dynamic damage model of crevasse opening and application to glacier calving. *Journal of Geophysical Research: Solid Earth, 110*(B1). doi:10.1029/2004jb003104

Pralong, A., Hutter, K., & Funk, M. (2006). Anisotropic damage mechanics for viscoelastic ice. *Continuum Mechanics and Thermodynamics, 17*(5), 387-408. doi:10.1007/s00161-005-0002-5

Qi, W. D., & Bertram, A. (1999). Anisotropic continuum damage modeling for single crystals at high temperatures. *International Journal of Plasticity, 15*(11), 1197-1215. doi:10.1016/s0749-6419(99)00035-2

Rignot, E., Jacobs, S., Mouginot, J., & Scheuchl, B. (2013). Ice-Shelf Melting Around Antarctica. *Science, 341*(6143), 266-270. doi:10.1126/science.1235798

Rignot, E., & MacAyeal, D. R. (1998). Ice-shelf dynamics near the front of the Filchner—Ronne Ice Shelf, Antarctica, revealed by SAR interferometry. *Journal of Glaciology, 44*(147), 405-418. doi:10.3189/S0022143000002732

Robinson, N. J., Williams, M. J. M., Barrett, P. J., & Pyne, A. R. (2010). Observations of flow and ice-ocean interaction beneath the McMurdo Ice Shelf, Antarctica. *Journal of Geophysical Research: Oceans, 115*(C3). doi:10.1029/2008jc005255

Scambos, T. A., Bohlander, J. A., Shuman, C. A., & Skvarca, P. (2004). Glacier acceleration and thinning after ice shelf collapse in the Larsen B embayment, Antarctica. *Geophysical Research Letters, 31*(18). doi:10.1029/2004gl020670

Schoof, C. (2005). The effect of cavitation on glacier sliding. *Proceedings of the Royal Society A: Mathematical, Physical and Engineering Sciences, 461*(2055), 609-627. doi:10.1098/rspa.2004.1350

Shepherd, A., Wingham, D., Payne, T., & Skvarca, P. (2003). Larsen ice shelf has progressively thinned. *Science, 302*(5646), 856-859. doi:10.1126/science.1089768

Stern, A. A., Adcroft, A., & Sergienko, O. (2016). The effects of Antarctic iceberg calving-size distribution in a global climate model. *Journal of Geophysical Research: Oceans, 121*(8), 5773-5788. doi:10.1002/2016jc011835

Stern, A. A., Johnson, E., Holland, D. M., Wagner, T. J. W., Wadhams, P., Bates, R., . . . Tremblay, J.-E. (2015). Wind-driven upwelling around grounded tabular icebergs. *Journal of Geophysical Research: Oceans, 120*(8), 5820-5835. doi:10.1002/2015jc010805

Sun, S., Cornford, S. L., Moore, J. C., Gladstone, R., & Zhao, L. (2017). Ice shelf fracture parameterization in an ice sheet model. *The Cryosphere, 11*(6), 2543-2554. doi:10.5194/tc-11-2543-2017

Todd, J., & Christoffersen, P. (2014). Are seasonal calving dynamics forced by buttressing from ice mélange or undercutting by melting? Outcomes from full-Stokes simulations of Store Gletscher, West Greenland. doi:10.5194/tc-8-2353-2014

Weertman, J. (1977). Penetration Depth of Closely Spaced Water-free Crevasses. *Journal of Glaciology, 18*(78), 37-46. doi:10.3189/S0022143000021493

Weis, M. (2001). *Theory and Finite Element Analysis of Shallow Ice Shelves.* (PhD). Technische Universität Darmstadt, Retrieved from http://tuprints.ulb.tu-darmstadt.de/171/

Yu, H., Rignot, E., Morlighem, M., & Seroussi, H. (2017). Iceberg calving of Thwaites Glacier, West Antarctica: full-Stokes modeling combined with linear elastic fracture mechanics. *The Cryosphere, 11*(3), 1283. doi:10.5194/tc-11-1283-2017

Zolochevsky, A., Sklepus, S., Hyde, T. H., Becker, A. A., & Peravali, S. (2009). Numerical modeling of creep and creep damage in thin plates of arbitrary shape from materials with different behavior in tension and compression under plane stress conditions. *International Journal for Numerical Methods in Engineering, 80*(11), 1406-1436. doi:10.1002/nme.2663